

## Source location using time-reverse imaging

Brad Artman\*, Igor Podladtchikov and Ben Witten

*Spectraseis AG, Giessereistrasse 5, 8005 Zurich, Switzerland*

Received June 2009, revision accepted June 2010

### ABSTRACT

We present the chain of time-reverse modeling, image space wavefield decomposition and several imaging conditions as a migration-like algorithm called time-reverse imaging. The algorithm locates subsurface sources in passive seismic data and diffractors in active data. We use elastic propagators to capitalize on the full waveforms available in multicomponent data, although an acoustic example is presented as well. For the elastic case, we perform wavefield decomposition in the image domain with spatial derivatives to calculate  $P$  and  $S$  potentials. To locate sources, the time axis is collapsed by extracting the zero-lag of auto and cross-correlations to return images in physical space. The impulse response of the algorithm is very dependent on acquisition geometry and needs to be evaluated with point sources before processing field data. Band-limited data processed with these techniques image the radiation pattern of the source rather than just the location. We present several imaging conditions but we imagine others could be designed to investigate specific hypotheses concerning the nature of the source mechanism. We illustrate the flexible technique with synthetic 2D passive data examples and surface acquisition geometry specifically designed to investigate tremor type signals that are not easily identified or interpreted in the time domain.

**Key words:** Diffractor, Sigsbee, Source location, Time-reverse modelling, Wavefield propagation.

### INTRODUCTION

Locating subsurface seismic sources is a problem common to a variety of geophysical experiments at all scales. Sources include earthquakes, subduction zone tremors (Shelly, Beroza and Ide 2007), volcanic tremors (Metaxian, Lesage and Dorel 1997) and stimulated events during fracture (Grechka, Mazumdar and Shapiro 2010), production (Maxwell and Urbancic 2001), or CO<sub>2</sub> storage (Maxwell, White and Fabriol 2004). Identifying and characterizing source locations is pivotal for evaluating the observations of increased tremor-like energy associated with reservoirs (Saenger *et al.* 2009; Riahi *et al.* 2009). The non-destructive testing community has an

extensive literature addressing the source location problem as well (Berryman 2002). Diffractor imaging is accomplished with the same kinematic processing algorithms as source imaging because both are described by only the one-way travelpath from diffractor or source to the seismic array. Diffractor imaging has been presented to locate structural (Berkovitch *et al.* 2009; Zhu and Wu 2010) or anthropogenic (Walters *et al.* 2009) discontinuities in seismic data and ground-penetrating radar (Feng and Sato 2004). The algorithm presented here is applicable to all of the location problems listed above.

In contrast to reflection migration, source location is a problem with only a single travelpath from the subsurface to receivers. We present a migration-like algorithm to locate subsurface sources in physical space. Our method is especially suited for location and characterization of sources with complicated wavelets and/or low signal-to-noise ratio superposed

---

\*E-mail: brad.artman@spectraseis.com

wavefields that are not interpretable in the data domain (van Mastrigt and Al-Dulaijan 2008; Lokmer *et al.* 2009). Under such conditions, earthquake-style event triangulation methods may struggle to produce reliable locations, while the stacking power of migration-like imaging techniques have potential to succeed (Chambers *et al.* 2008). Like reflector imaging, our proposed method requires an accurate interval velocity model as input.

Time-reverse modeling is the starting point for this work (Fink 1999). Time-reverse processing entails simply propagating a wavefield through a velocity model after reversing the time axis. We present examples using both one-way acoustic (Gazdag and Sguazzero 1985) and finite difference elastic propagation schemes (Saenger, Gold and Shapiro 2000). Both have been implemented by the authors. The basics are simple: time-reversed data are injected into the model domain as sources at recording stations and propagation causes events to focus at the source location.

This presentation extends reverse-propagation processing schemes (Gajewski and Tessmer 2005) to an explicit imaging methodology (Norton and Won 2000; Steiner, Saenger and Schmalholz 2008) with the addition of physically meaningful elastic imaging conditions. The complete algorithm is the chain of reverse propagating data, spatial processing to separate  $P$  and  $S$  energy and evaluating imaging conditions to collapse the time axis. These three steps image source locations in physical space. This chain of operations we name time-reverse imaging. The images produced by multiple elastic imaging equations are interpretable with respect to source mechanism and orientation.

With only a single transmission wavefield from a passive seismic data volume, we calculate the zero-lag of the autocorrelation over time at every model location  $(x, z)$  after propagation. This is similar to illumination compensation in reflection migration (Jacobs 1982). The zero-lag of a correlation captures the energy of collocated events in space and time (Claerbout 1971). Large values of the zero-lag of the correlation, which is proportional to the variance for zero-mean data, indicate deviation from random noise and the presence of an event (Melton and Bailey 1957).

We capitalize on elastic processing and introduce correlation imaging conditions between  $P$  and  $S$  potential wavefields similar to reflector/converter imaging (Wapenaar, Kinneging and Berkhout 1987; Yan and Sava 2008). While several specific imaging conditions are presented, we advocate a general philosophy of ‘image-domain processing’, whereby multiple imaging conditions are evaluated, each designed to image various physical mechanisms or wavefield components. This ap-

proach produces a suite of images to be compared and contrasted to interpret finer details about the source mechanism beyond just its location in space.

In the first section we briefly explain the kinematics of reverse propagation and introduce the autocorrelation imaging condition to locate subsurface sources. Second, we apply the acoustic algorithm on a synthetic marine data set with the added complication that targeted diffraction events are embedded within a reflection wavefield. The third section explains the wavefield decomposition method that facilitates vector imaging conditions. Fourth, we demonstrate the impulse response of the full elastic imaging algorithm with various simple source mechanisms including oriented single point forces and the double couple in a homogeneous medium. Finally, we present a complex synthetic example with a swarm of sources in a realistic earth model. Our examples are all 2D, though the 3D extension is algorithmically trivial. We do not consider the effects of anisotropy in this presentation of basic principles, though the algorithm can readily be extended (Yan and Sava 2009).

Our methodology can be implemented for arbitrary acquisition geometries, though the examples we present are developed with surface acquisition. The main advantages of this imaging methodology will be realized for surface arrays with large numbers of stations. Therefore, we do not consider the limited station borehole experimental geometries. Most of the examples presented are developed toward investigating whether observations of tremor type signals in surface arrays can be associated with specific subsurface locations at depth (Saenger *et al.* 2009; Lambert *et al.* 2009).

## FOCUSING BY PROPAGATION

The time-reverse modelling algorithm was developed for locating sources emanating from within a well characterized domain (Fink 1999; Fouque *et al.* 2007). Figure 1 shows the simple kinematic surface of an acoustic energy source in a homogeneous space-time domain. A hyperbolic event is recorded in the data as function of surface location and time,  $d(x, t)$ , at depth  $z = 0$ . The extrapolation direction is defined here as  $z$ . To collapse the event to its subsurface source location, we first reverse the data in time and perform the 2D Fourier transform of the data,  $D(k_x, \omega)|_{z=0} = \text{FFT}_{x,t} [d(x, -t)]|_{z=0}$ . The depth axis is built by recursive propagation

$$D(k_x, z + \Delta z, \omega) = D(k_x, z, \omega) e^{-i\Delta z k_z}, \quad k_z = \sqrt{\omega^2 s^2 - k_x^2}. \quad (1)$$

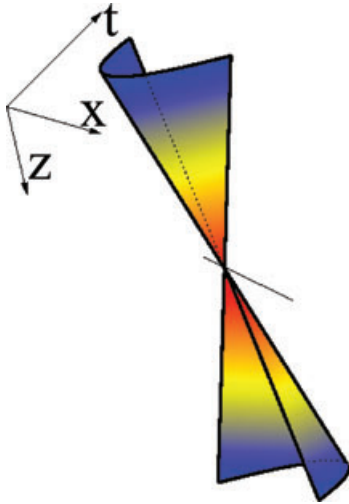


**Figure 1** Simplified propagation surface in the combined space-time domain. Hyperbolae are extracted in any  $x$ - $t$  plane. Source location is at the intersection of the two cones. Hot colours reflect increased amplitude due to constructive interference.

Angular frequency is  $\omega$ ,  $s$  is the medium slowness,  $\Delta z$  is the depth sampling interval and  $k$  are the spatial wave numbers. The recorded event collapses to a focus at the intersection of the two cones in Fig. 1. Without knowledge of where to insert sink locations, since finding such locations is the goal of the imaging method, a focus is subsequently expanded with further extrapolation steps.

The increasingly warm colours toward the source location indicate the increased energy at those model locations due to constructive interference as the event collapses. As the energy from individual stations is focused in the model space, the implicit summation of focusing is the reason that the image signal-to-noise ratio is improved compared to the data measure. Kinematically, focus occurs when all the planar segments of an arrival collapse to a common location in space-time. Accuracy and resolution of the image is dominantly controlled by the velocity model. A poor velocity model mislocates and smears the focus. Given an accurate model, the resolution of the focus is then controlled by frequency content and the completeness of the set of planar components included in the data. For surface arrays, this highlights the importance of aperture. The lack of data from below the source causes an extended smear of energy in the direction normal to the array. This is the ‘range resolution’ problem in non-destructive testing (Borcea, Papanicolaou and Tsogka 2003). Arrays that do not record both positive and negative ray parameters from an event cause a too shallow energy maximum and lateral smear of energy in the image.

After creating the depth axis from the time data by propagation, the geophysicist must decide how to use the larger data volume. Our method will only locate the source in physical space, such that onset time (a typical source parameter in event triangulation methods) is lost. However, coarse resolution of the time parameter is available by selection of time windows for imaging.

To create an image as a function of space, we calculate the zero-lag of the autocorrelation at every spatial location (Artman and Podladtchikov 2009). Previous authors have suggested other measures, such as the maximum or average amplitudes over time (Steiner *et al.* 2008; Lokmer *et al.* 2009). Though similar, the maximum amplitude measure captures only the peak amplitude time sample of a source wavelet. Simple sums over time suffer for zero-mean data by not capturing total energy content. We advocate the zero lag of a correlation (proportional to the variance for zero-mean data), for several reasons. First, large values of variance indicate the presence of an event (Melton and Bailey 1957), which is our goal. Also, correlations collapse complicated waveforms and capture the total energy of every event in the data. Further, this choice conforms to the existing migration canon (Claerbout 1971). The zero-lag of the autocorrelation is simply accumulated over propagation time or frequency by

$$i(x, z) = \text{iFFT}_{k_x} \left[ \sum_{\omega} D(k_x, z, \omega) D(k_x, z, \omega)^* \right] = \sum_t d(x, z, t)^2, \quad (2)$$

where the form of the propagator used dictates whether Fourier or time domain equivalents are more convenient.

All traces at the acquisition surface contain the event and therefore have measurable autocorrelation or variance. As the event collapses down the cone in Fig. 1, spatial locations away from the source at  $z > 0$  lose the event and have small variance over time. At the source location, the accumulation of energy leads to large variance. The chain of propagating time-reversed data with equation (1) and applying the imaging condition in equation (2) is the wave-equation implementation of similar Kirchhoff algorithms also in the literature (Chambers, Barkved and Kendall 2009).

## EMBEDDED ONE-WAY WAVE FIELDS

Diffractions within active seismic data are examples of one-way wavefields embedded within two-way wavefields (Khaidukov, Landa and Moser 2004). Despite the presence of the reflections in the data, diffractors can be located with the time-reverse imaging methodology. The stationary phase

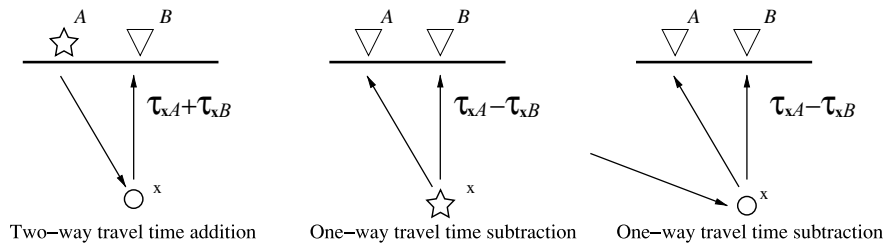


**Figure 2** Triangles are receivers, stars are sources, circles are diffractors. A, B and x are the locations and rays represent traveltimes,  $\tau$ , in equations (3) and (4). Left corresponds to the reflection experiment and equation (3). Both the subsurface source and an externally stimulated diffractor (centre and right) are imaged with equation (4).

summation surface, or migration kernels, for reflector and diffractor imaging are presented in both Schuster *et al.* (2004) and Borcea, Papanicolaou and Tsogka (2006). For reflection migration, the summation surface corresponds to the sum of the travelpaths,  $\tau$ , from location A to subsurface model point  $\mathbf{x} = (x, z)$  and back to surface location B

$$i_r(\mathbf{x}) = \sum_{A,B} d(A, B) e^{-i\omega(\tau_{xA} + \tau_{xB})}. \tag{3}$$

In contrast, source imaging kernels sum across surfaces defined by the one-way time differences between the path from x to A and the path from x to B, such that

$$i_s(\mathbf{x}) = \sum_{A,B} d(A, B) e^{-i\omega(\tau_{xA} - \tau_{xB})}. \tag{4}$$

Figure 2 cartoons the raypaths  $\tau_{xB,A}$  corresponding to the summation surfaces in the above equations. On the left is the down-up travelpath corresponding to the migration sum in equation (3). The centre diagram shows the rays emanating from a subsurface source that is imaged with equation (4). The summation surface in equation (4) is the same as presented by the geometric construction in Dobrin (1952) for calculating ‘step-out time’ between receivers for a reflection from a dipping layer, as shown in the right schematic. The incoming ray could be from the surface, or ambient seismic energy travelling at depth.

Figure 3(a) is a migration produced with acoustic extrapolators applied to the Sigsbee2b synthetic data. The data are a freely available acoustic towed streamer synthetic (SMAART 2002). The image was produced by shot migration (Claerbout 1971) with Fourier-domain wave-equation extrapolation (Gazdag and Sguazzero 1985). This wave-equation migration corresponds to the ray-theory migration kernel in equation (3). White arrows at the sea floor point to discontinuities in the model due to implementing dipping reflectors with a Cartesian finite-difference grid. The model includes strings of diffractors across two depth levels (arrows at  $z =$

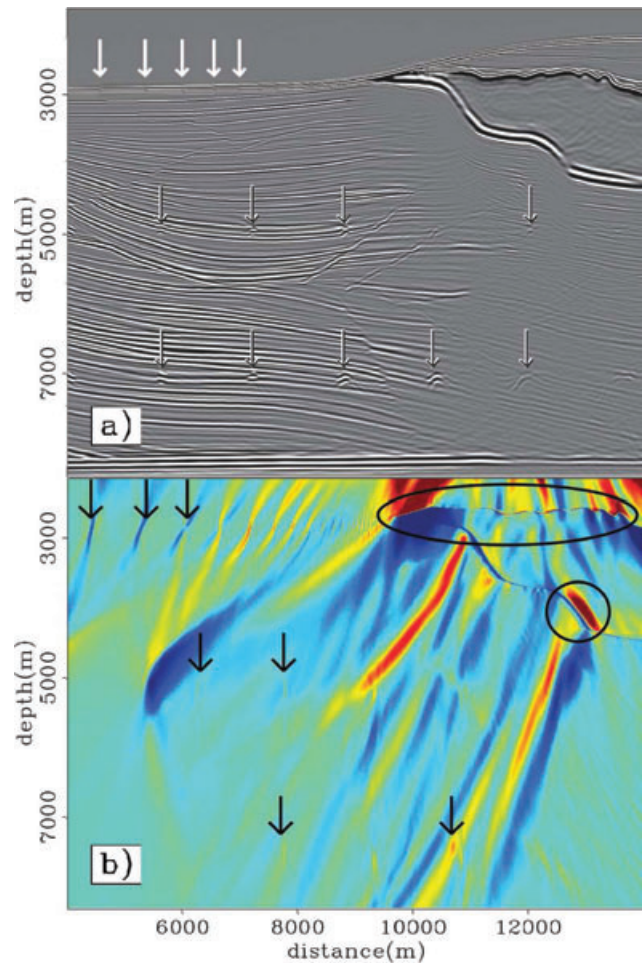


**Figure 3** a) Wave-equation migration of the Sigsbee2b data. Arrows point to step discontinuities in the dipping sea-bottom and deep diffractors. b) Time-reverse image of the same data.

5000, 7000 m, which we attempt to locate in space with the time-reverse imaging algorithm.

The image in Fig. 3(b) is produced by propagating the time-reversed data, equation (1) and applying the imaging

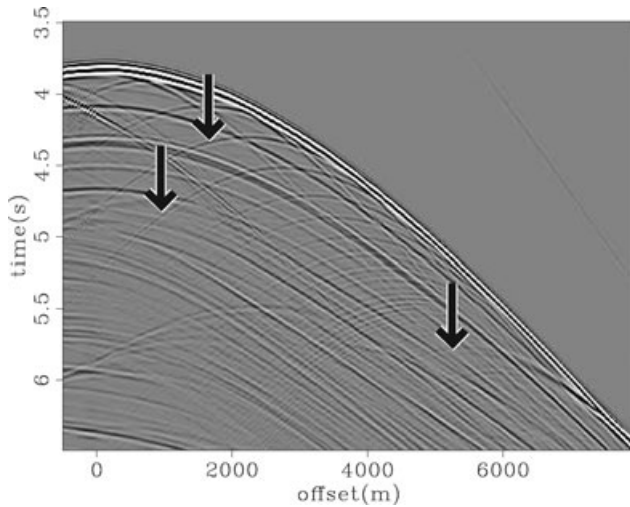


**Figure 4** Shot gather from the Sigsbee2b data with some arrows pointing to diffraction modelling artefacts. Hyperbolic events with both limbs in this one-sided gather are predominantly diffractions.

condition in equation (2). This wave-equation source imaging corresponds to the ray-theory diffractor kernel in equation (4). Post-processing was AGC. Arrows point to the first three of a series of foci across the water bottom and a few of the diffractors across  $z = 5000, 7000$  m. The sigmoidal shape of the diffraction foci on the sea-bottom shows the impulse response of off-end acquisition. They are centred at the steps imaged in Fig. 3(a) indicated by white arrows. The circles highlight strong, very dense energy accumulations along the steep salt flanks.

Although the deep diffractors were the targets we were attempting to image, many more diffractors were imaged in the shallow section of the data. Figure 4 shows 3 seconds after the sea floor reflection of a representative shot gather. Nearly every reflection and especially the strong sea floor and salt events, are highly contaminated by diffractions that are modelling artefacts. The effects of the Cartesian grid used for finite-difference forward modeling of dipping horizons are obvious in the migration (Fig. 3a), the diffractor image (Fig. 3b), and the data (Fig. 4).

## VECTOR PROCESSING IN THE IMAGE DOMAIN

Historically, acquisition plane processing has been relied on for wavefield decomposition (Zhe and Greenhalgh 1997; Dellinger, Noite and Etgen 2001) for most multicomponent data processing. In the case of low signal-to-noise ratio one-way wavefields, the required information to perform the pre-

processing correctly is likely not available. Instead, we implement the full elastic solution to the wave equation for reverse propagation. Doing so incurs a substantial increase in computational burden but simplifies preprocessing to only a band-pass operation. Multicomponent data,  $\mathbf{d}$ , are source functions for propagating wavefield  $\mathbf{u}(x, z, t)$  that satisfies

$$\rho \ddot{\mathbf{u}} - (\lambda + 2\mu) \nabla \nabla \cdot \mathbf{u} + \mu \nabla \times \nabla \times \mathbf{u} = \mathbf{d}(x, z = 0, -t). \quad (5)$$

Medium parameters density,  $\rho$  and Lamé parameters,  $\lambda$  and  $\mu$ , must be available from external sources. We implement time-domain elastic propagation after Saenger *et al.* (2000).

Simple vector identities extract single propagation modes from the total wavefield (Aki and Richards 2002). The model domain after extrapolation is a regular and complete representation of the wavefield in space such that  $P - S$  separation does not require approximations for the vertical derivative (Huang and Milkereit 2007) or knowledge of source parameters. The compressional,  $E_P$  and shear,  $E_S$ , kinetic energy densities are (Morse and Feshbach 1953)

$$E_P = P^2 = (\lambda + 2\mu)(\nabla \cdot \mathbf{u})^2, \quad \text{and} \\ E_S = |\mathbf{S} \cdot \mathbf{S}| = \mu(-\nabla \times \mathbf{u})^2. \quad (6)$$

These relations are strictly valid in the far-field for body wave modes in isotropic media. The wavefields  $P$  and  $\mathbf{S}$  have preserved sign information (zero mean) that captures the relative amplitudes within the propagation modes (Dougherty and Stephen 1988). The energy quantities  $E$  are strictly positive due to squaring (the inner product for  $\mathbf{S}$ ). In 2D, the vector  $\mathbf{S}$  has only one non-zero entry that is physically the  $S_v$ -wave.

Figure 5 illustrates the collapse of energy from a source at depth recorded at the surface via reverse propagation of the elastic wavefield in a homogeneous medium. The panels are all extracted from the extrapolation time axis at the initiation time of a vertical single force point source in an elastic medium. This means no automatic imaging condition has been applied but we have exploited knowing the onset time of the source in the synthetic. The goal of an automatic imaging condition is to extract images similar to these without needing to know the time of occurrence.

Figure 5(a) is the absolute amplitude of the multicomponent wavefield. Panels b and c are the  $P$  and  $S_v$  wave potentials by equation (6). The source is located at the maximum amplitude of panel a and at the zero crossings in the centres of panels b and c. Longer wavelengths are seen on the  $P$  image due to faster propagation velocity. Several artefacts are present in the potential wavefields that are non-physical or due to limited aperture acquisition (Yan and Sava 2008). The extra events on panel b are limited aperture artefacts. They are  $P$ -wave

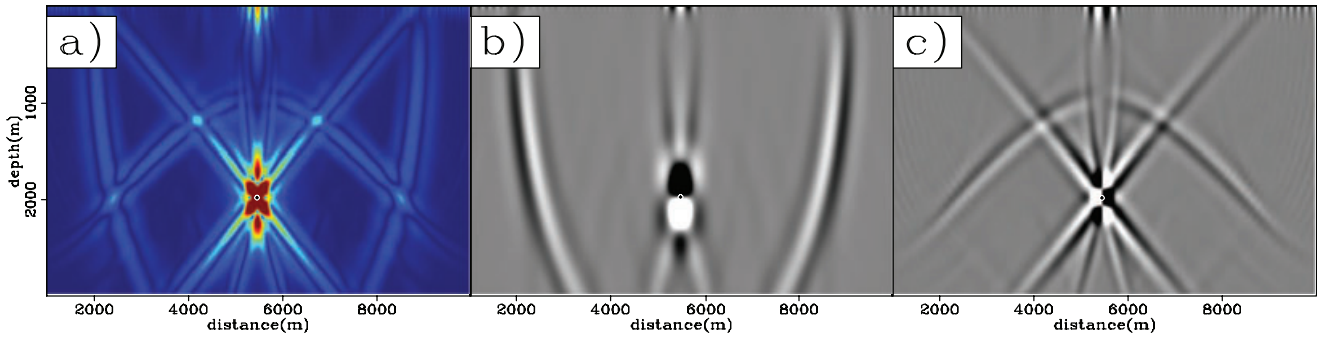


**Figure 5** Wavefield snapshots after reverse propagation to the initiation time of a vertical point single force. Panel a is absolute amplitude. Panels b and c are the  $P$  and  $S$  potential wavefields by equation (6). The radiation pattern is apparent around the source location dots.

conversions from the truncated tips of the  $S$ -wave hyperbola. The linear events on panel c are non-physical artefacts from the node, or zero crossing, at the top of the  $S$ -wave hyperbola. The hyperbola on panel c is the  $P - S$  conversion from the free surface. Panels b and c show the spatial radiation pattern of positive and negative amplitudes in addition to the source location at the energy maximum in panel a, as also noted by Lokmer *et al.* (2009).

## ELASTIC TIME-REVERSE IMAGING

Decomposing the vector wavefield into physically meaningful scalars allows the development of several cross-correlation imaging conditions in extension to the acoustic case presented above. As suggested in Steiner (2009), we calculate the spatial derivatives, equation (6), before the imaging condition to compute the scalar potential wavefields from the vector wavefield. We introduce cross-correlation of the wavefield components  $P$  and  $S$  to image sources, which is similar to  $PS$  converted wave migration (Wapenaar *et al.* 1987; Yan and Sava 2008). The  $PS$  image of a subsurface source is

$$I_{PS}(x, z) = \sum_t P(x, z, t)S(x, z, t), \quad (7)$$

where a scalar potential  $S$  is selected or calculated from the vector  $\mathbf{S}$  in equation (6). In 3D there are several potential choices from  $\mathbf{S}$ . A wavefield component of  $\mathbf{S}$  can be used for imaging individually, for example  $PS_v$ . Or, a combination of wavefields can be calculated, such as  $S_b$  from the two horizontal components.

The  $PS$  imaging condition passes forward scattering mode conversions (Shragge, Artman and Wilson 2006) since both potentials in the imaging condition are derivatives of a single up-coming multicomponent wavefield,  $\mathbf{u}$ . Single wavefield

autocorrelations can be calculated as well, analogous to the acoustic case in equation (2), to produce  $PP$  and  $SS$  images. Further, correlations of the energy density functions,  $E_P$  and  $E_S$  from equation (6), will also have some advantages discussed later. Regardless of dimensionality,  $E_S$  is a scalar containing the combined energy of all  $S$ -waves.

The  $PS$  imaging condition for source location exploits the fact that the  $P$ - and  $S$ -waves propagate at different speeds. The near field is defined by the distance of propagation required to fully separate  $P$  and  $S$  wavelets in space and time. In the near-field, as discussed in Aki and Richards (2002, 4.2.3), the source is simultaneously both  $P$  and  $S$ : source energy maps through both the divergence and curl operators in equation (6). The zero-lag of the cross-correlation images the source energy in the vicinity around the source that corresponds to the near-field, where  $P$ - and  $S$ -waves are uniquely collocated in space and time.

The impulse response of the experiment is greatly affected by the acquisition geometry and source mechanism. Therefore, we present a suite of images from synthetic point sources to show the impulse response of various mechanisms: the horizontal double couple and vertical,  $45^\circ$  and horizontal single forces. These images compose a dictionary of impulse responses with which field data results can be compared.

The data synthesis and imaging propagation steps were all performed in a homogeneous model with compressional velocity  $v_p = 3000$  m/s, Poisson's ratio  $\nu = 0.3$ , density  $\rho = 2000$  kg/m<sup>3</sup>, sampled at 10 m in all directions. We used a Ricker wavelet time function with dominant frequency 4 Hz. The low-frequency content was selected specifically to investigate the ability of the method to image tremor signals (Shelly *et al.* 2007; van Mastrigt and AlDulaijan 2008). Data were simulated with mildly irregular,  $\sim 900$  m, receiver spacing to represent field conditions.

### Vertical single point force

Figure 6 are all time reverse images of data modelled from a vertical single point force in a homogeneous model with various imaging conditions. These images are the system response of the surface acquisition and source mechanism. All images are scaled to one. Panels a and b are the zero-lag of the autocorrelations of  $P$  and  $S$  potential wavefields and Fig. 6(c) is their cross-correlation. The single mode images are strictly positive, while the  $PS$  image has zero mean. In panels b and c, the  $S$ -wave nodal plane in the radiation pattern of the vertical force causes the zero-crossings in the  $SS$  and  $PS$  images. The horizontal nodal plane in the  $P$  radiation pattern is not sampled by the surface array. Because the image results are the sum of potential wavefield multiplications over all time (equation (7)), Fig. 6 images are not exactly multiplications of the  $P$  and  $S$  radiation patterns in Fig. 5(b,c). However, shapes observed in all the images can be interpreted as such for a basic understanding.

The source location in Fig. 6(c) is at the location of the zero crossing at the black dot. The anti-symmetric clover-leaf pattern surrounding the source identifies its location. The area within the clover pattern is the near-field region where  $P$  and  $S$  wave energy is collocated. The antisymmetric pattern in the  $PS$  image suggests simple post-processing to identify the source position with a maximum instead of the multi-dimensional zero crossing. A  $\pm 90^\circ$  phase rotation in both directions of

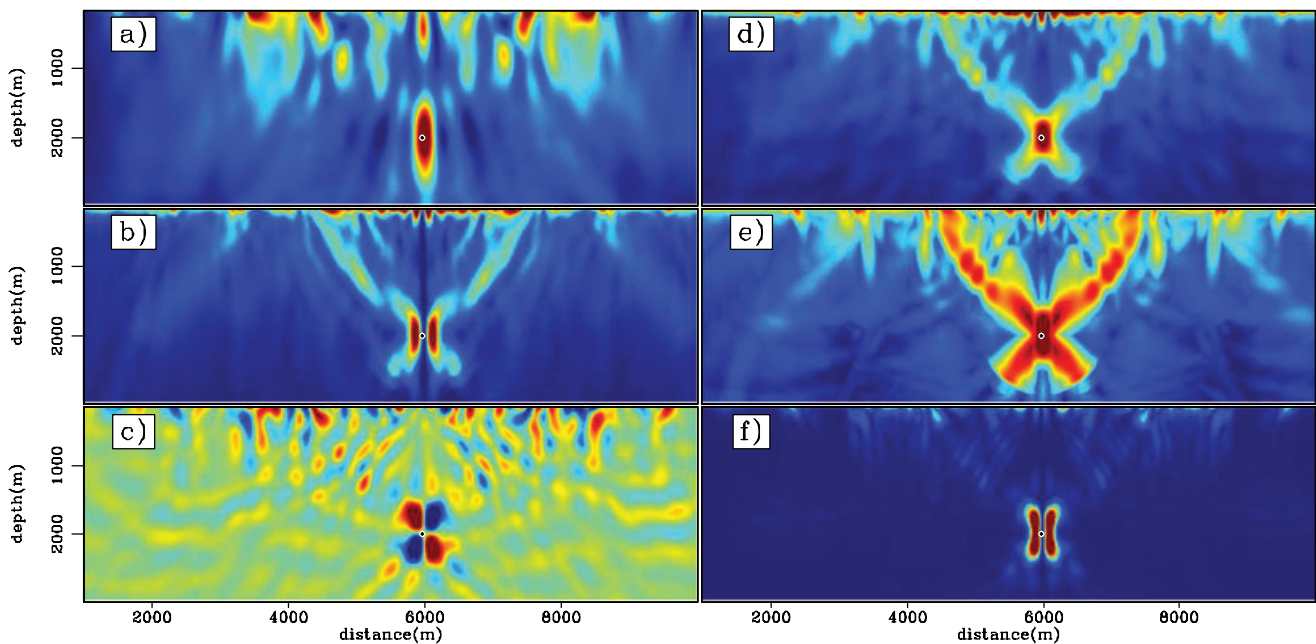
the image with a 2D spatial integral or derivative of panel c will result in a maximum at the location of the dot. This post-processing will be shown in a later example.

Figure 6(d) is zero-lag of the autocorrelation of the absolute amplitude over all propagation time. This is approximately the square of panel e, which is the maximum absolute amplitude over all time (Steiner *et al.* 2008). These are included largely as comparisons to previous work. For single source simple synthetics, most imaging conditions work adequately. However, there is clear uplift in the quality and information content in the suite of images in panels a–d compared to panel e. Correlation imaging conditions outperform sums and maximums for complex wavelets with long codas and when multiple events are in the same wavefield.

Panel f is the zero-lag of the cross-correlation between the energy density functions  $E_P E_S$ . Panel f is approximately the square of panel c, as will be expected from the potential separation equation (6). However, in the case of complicated super-posed wavefields, the squared energy-density imaging condition is more stable. Squaring penalizes small numbers that are likely cross-talk and artefacts.

### 45° single point force

The specific radiation patterns of source functions will resolve differently in the three principle images,  $PP$ ,  $SS$  and  $PS$ . As



**Figure 6** Images of a vertical single point force. Panels a, b and c are  $PP$ ,  $SS$  and  $PS$  respectively. Panel d: autocorrelation of the absolute amplitude. Panel e: maximum over all time. Panel f:  $E_P E_S$ . Dots indicate point source location.

such, we provide results using the same imaging conditions and continue accumulating the image dictionary of source functions. Given a sparse acquisition and propagation effects from the velocity structure, it is important to model impulse response images with field parameters for several potential source mechanisms to be able to interpret source parameters from field data.

The panels in Fig. 7 are the elastic data modelled from a single point force oriented  $45^\circ$  anti-clockwise. The oriented point force has an unbalanced energy distribution between the limbs of the hyperbolas due to the radiation nodes of the single force. The  $P$  energy is predominantly on the left stations and the opposite is true for the  $S$  arrival. The arrivals on the traces at the edges of the domain are separated in time by approximately one wavelength between neighbouring traces.

Figure 8 shows the images from data in Fig. 7. The panels are  $PP$ ,  $SS$  and  $PS$  images respectively. The right column of images shown in Fig. 6 are left off for brevity. The  $PP$  image in panel a shows only weak focusing compared to the other images. The lateral distribution of energy and relative amplitudes of the events in Fig. 7 explain the tilted focus patterns at the source location in the images. Although the source location is identified in the  $PP$  result, the impulse response is a little weaker than some of the artefacts in the shallow section. If some knowledge of the expected source depth interval is available, this may not be detrimental. Similar observations can be made in the remaining images, although the  $SS$  and  $PS$  images are superior for this source mechanism.

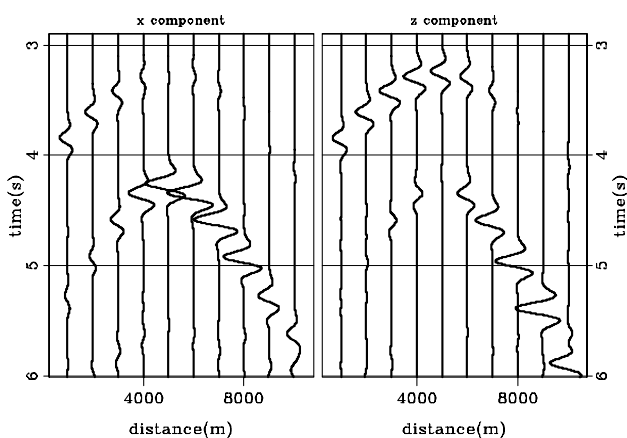


Figure 7 Data modelled from a single point force oriented  $45^\circ$  anti-clockwise. Left is the horizontal component and right is the vertical component.

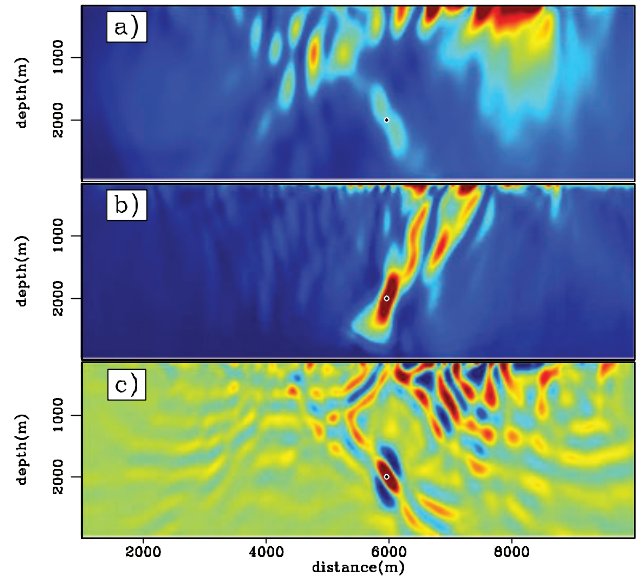


Figure 8 Images of a  $45^\circ$  oriented single point force. Panels a, b and c are:  $PP$ ,  $SS$  and  $PS$ . Dots indicate point source location.

#### Horizontal single point force

Figure 9 shows images of a horizontal single point force. The panels are again:  $PP$ ,  $SS$ ,  $PS$  images. The focus patterns of the same panels in Fig. 6 due to the  $90^\circ$  rotation of the source radiation patterns. There are two reasons that the amplitude of the  $P$ -wave focus in panel a is not as high as the  $S$ -wave focus

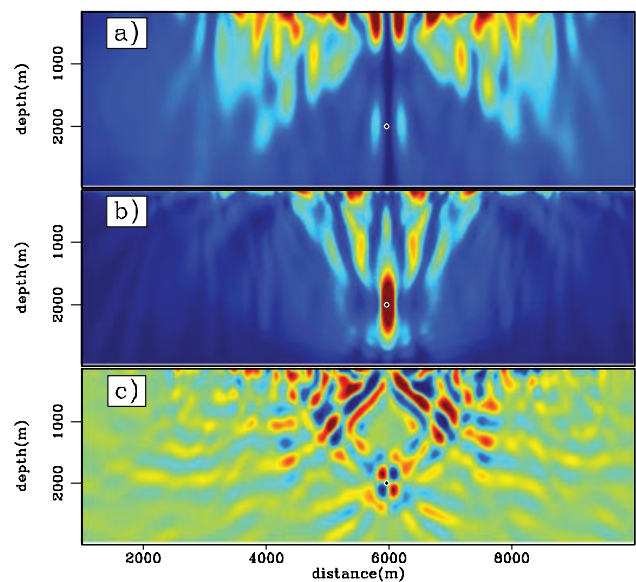


Figure 9 Images of a horizontal single point force. Panels a, b and c are:  $PP$ ,  $SS$  and  $PS$ . Dots indicate point source location.



in Fig. 6(b). First, the amplitudes scale with slowness. Second, the surface array is centred over the  $P$ -wave node. Panel c has tighter focusing due to the higher wavenumber content of the  $S$ -waves, as noticed in Fig. 5, which accounts for the bulk of the energy content in the data for this combination of acquisition geometry and source mechanism.

### Double couple point source

Figure 10 shows the impulse response of the  $PP$ ,  $SS$  and  $PS$  time-reverse images for a horizontal double couple point source. The source was modelled by seeding the  $xz$  components of the stress tensor with the source wavelet (Aki and Richards 2002; Schubert and Schechinger 2002). For this mechanism, the auxiliary  $P$ -wave node is vertical and the  $S$ -

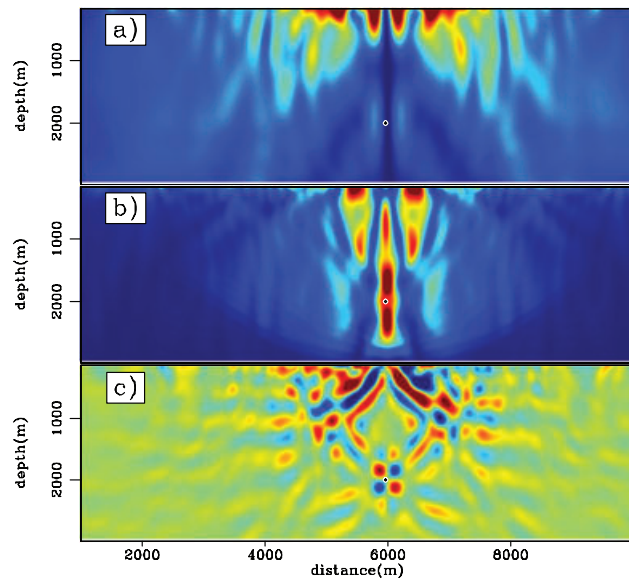


Figure 10 Imaging condition options for a horizontal double couple point force. Panels a, b and c are  $PP$ ,  $SS$  and  $PS$ , respectively. Dots indicate point source location.

wave radiation is maximum toward the surface. The double couple images are almost the same as those from the horizontal single force in Fig. 9. Because the surface array does not sample all quadrants of the radiation pattern there is very little difference between the two data sets.

### SOURCE SWARMS

Figure 11(a) shows a real  $P$ -wave velocity model used to forward model a source location experiment. Constant  $V_p/V_s$  ratio and density were used for this feasibility exercise. The circles at the top of panels b and c are receiver stations. The modelled data were produced with a swarm of 100 vertical single point forces indicated by the asterisks in panel c. Applying the same source mechanism at all locations implies a common external forcing mechanism or a common failure orientation. The radiation patterns of non-explosive sources have positive and negative lobes. Therefore, positive and negative interference will be expected even for aligned mechanisms. Ricker wavelet time functions with central frequency 4.5 Hz were randomly triggered up to 10 times along the time axis at each location. The goal was to generate time signals with so much cross-talk as to be uninterpretable and have the appearance of randomness (which was achieved). This is a model of a large area tremor-like signal (Shelly *et al.* 2007; van Mastrigt and Al-Dulaijan 2008) by the superposition of simple mechanisms.

Panel b is the  $PS$  image, equation (7), of the forward modelled swarm of sources. The complexities of irregular acquisition geometry, complex subsurface velocity and simultaneously imaging many sources introduce cross-talk artefacts in the image. However, most artefacts are confined to the upper 1200 m of the image. The feature at approximately 2300 m depth resembles the antisymmetric cloverleaf seen in the impulse response image in Fig. 6(c). Even though more than

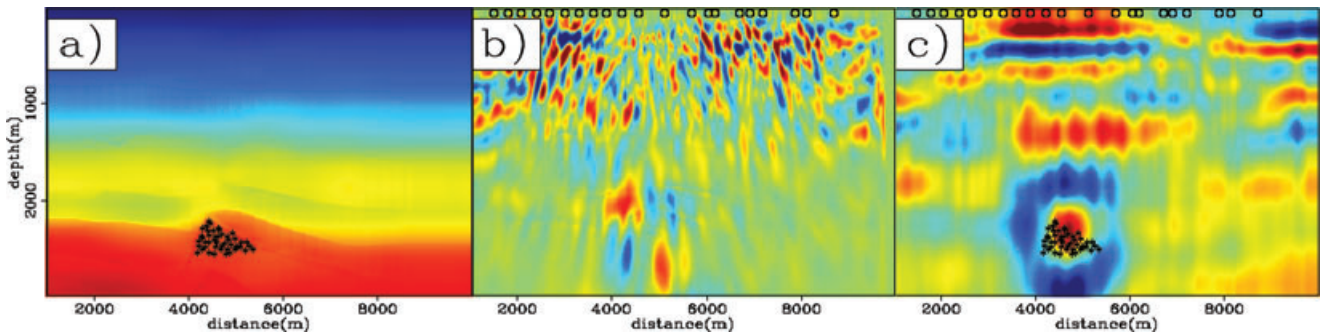


Figure 11 Velocity model (a) and  $PS$  time-reverse images before (b) and after (c) 2D spatial integration. Irregular data acquisition shown with circles at the surface. Source locations at depth shown by asterisks.

500 individual sources were processed simultaneously in a complex wavefield, we still retain an identifiable feature in the image that can be related to the impulse response tests shown above.

The location of the centre of mass of the source swarm is at the fairly broad zero crossing in panel b. Again, the radiation pattern of energy has been imaged. As suggested above, discussing Fig. 6(c), a  $90^\circ$  phase rotation in  $x$  and  $z$  directions will transform the antisymmetric clover into a single maximum. Both integration or differentiation result in a  $90^\circ$  phase rotation. They are simply implemented in the Fourier domain by division or multiplication, respectively with  $(-k_x k_z)$ . We have found that for complex and noisy data, the integration is more stable at the cost of a less compact focus.

Panel c is the 2D integration of panel b with the source locations overlain. While the 2D integration nicely images the centre of mass of the swarm of source events, the horizontal stripes above the sources introduced during the process could be misinterpreted. To avoid such pitfalls, post-processing suggested by synthetic models should be used with caution.

## DISCUSSION

We advocate the use of fully elastic time-domain wave-equation propagators when multicomponent data are available because a more complete solution to the underlying physics of propagation removes the need for many assumptions and preprocessing. Processing steps, such as wavefield decomposition, are instead performed after propagation in the image domain that enjoys more regular sampling and a complete depth axis. As in all imaging processes, the accuracy of the velocity model controls the quality and accuracy of the output. Small errors in  $v_p$  and  $v_s$  will cause smearing and incomplete focusing. More substantial errors can lead to no focusing at all. Assuming both  $P$  and  $S$  modes focus at the same depth location, mismatch and smear give some indication as to the quality of the velocity information. We assume that  $P$ -wave velocity fields from active seismic data are more accurate than the assumptions made to generate shear velocity profiles. Work is underway to fully investigate the effects of these inaccuracies.

Defining migration as a process of extrapolation followed by an imaging condition we can see that the source imaging technique can realistically be viewed as a migration algorithm addressing a different kinematic problem than concerns the reflection seismic community. Migration algorithms can be viewed as a physically tuned form of stack, which is possibly

the single most powerful concept in data processing. Focusing energy at locations in the model domain via propagation and then applying an appropriate imaging condition effectively sums the contribution from all receivers to the scatterer or source being imaged. Therefore, migration algorithms are especially beneficial when the data domain suffers from poor signal-to-noise ratio. A weak signal may be present and significant but not observable in the data until the cohesive contribution from all receivers is focused in space and time (Artman 2006). Second, phenomena can be difficult to observe in the data domain due to the convolution of a simple process with a long, complicated source function. Under such circumstances, correlation based imaging conditions offer substantial benefit by collapsing a coda to a compact wavelet.

A method to image events that are not detectable in the data domain can be especially powerful for event location in micro-seismic monitoring if the acquisition is appropriate. The power-law magnitude distribution of seismic events stipulates that for every increment down in magnitude we should expect about ten times as many smaller events (Gutenberg and Richter 1954). This leads to the understandable desire for greater hardware sensitivity, and installation as close as possible to the region of interest in order to collect ever more complete data sets. Regardless of how successful we are at engineering solutions for data acquisition, there should always be many more low signal-to-noise ratio events that we can try to find through the power of a physically tuned (wave-equation) stacking algorithm.

For limited aperture arrays, the horizontal resolution is much better than the vertical. Horizontal resolution is dictated most strongly by array aperture. Vertical resolution is mostly a function of the frequency content of the source. However, resolution can be considered in terms of both accuracy and precision. A single maximum (or zero crossing) location can be selected from the images that will be very precise. However, the accuracy should be considered in terms of standard quarter wavelength, or Fresnel zone arguments. As in all migration processing techniques, the method is a deterministic process whose accuracy is controlled by the correctness of the velocity model and the quality of the acquisition parameters used to initialize the wavefield propagation.

Due to the expense of elastic wave propagation, imaging by time-reverse modelling is probably not warranted if identifiable ballistic events are detectable in the data domain. Especially if data are collected with a very sparse (order ten) array with limited aperture, such as a borehole string, the stacking power of the migration algorithm may not provide as much added value to the location effort.

The effects of noise on the images can be deleterious. Migration-like processing increases the signal-to-noise ratio of the image compared to the data domain but spurious noise effects may cause false highs in an image. The ability to confidently interpret results with field data depends on a priori knowledge constraining realistic model locations, or the ability to mitigate spurious energy in images that may be caused by acquisition, noise, algorithm and/or the earth model. This presentation provides only the foundation on which to build toward those further goals. Correlation-based imaging conditions are powerful tools to collapse complicated waveforms. Calculating and interpreting non-zero lag image volumes, in time and or space (Vasconcelos, Sava and Douma 2009), might lead to better imaging and source parameter characterization, or even velocity model updates (Yang and Sava 2009).

The various imaging constructs we have presented are adjoint processing techniques (Claerbout 1985). Kawakatsu and Montagner (2008) presented a discussion on the current status of moment tensor inversion as compared to adjoint processing in the earthquake analysis community. While those authors contrast the two concepts, we think that our work can be a step toward bridging the two. Sources modelled with many different characteristics and imaging conditions have been shown to be sensitive to the source parameters. While we have argued for simply comparing models to field result, the problem should be amenable to be cast as an iterative inversion problem (Claerbout 1992) using some of the tools developed above. This would offer the ability to formally estimate source mechanism parameters as is commonly done in moment tensor analysis (Eshelby 1957; Heaton and Heaton 1989) after having removed propagation effects from the data.

## CONCLUSIONS

We use the chain of multicomponent acquisition, elastic propagation, wavefield decomposition and correlation imaging conditions to locate subsurface sources and diffractors. We name the algorithm time-reverse imaging. The method actually images the near-field source radiation pattern rather than a simple energy maximum at the source location. The method is very similar to making illumination maps (Jacobs 1982) with a data wave field in reverse time migration (Levin 1984).

Input data are only bandpassed and reversed in time before imaging, requiring no knowledge of any source parameters. Decomposition into  $P$  and  $S$  potential wavefields is performed in the image domain at every time propagation step. Thus,

multiple potential wavefields are available to combine by a suite of imaging conditions. Source initiation time does not enter into the formulation of the method at any stage, so although the lack of knowledge of when a source initiates does not affect the result, neither is initiation time a parameter that can be estimated. No picking in the data domain is required. Accurate interval velocities of the subsurface are required as input for the imaging method.

An important feature of this method is the correct handling of  $P$ - and  $S$ -wave arrivals without any preprocessing or assumptions. For the presented horizontal single force and double couple, most of the energy on the records is likely to be from  $S$ -wave arrivals, while the  $P$  arrival may not be easily observable. If  $S$  energy is imaged with acoustic far-field extrapolators and  $P$ -wave velocity, it will focus at the wrong location. Thus, we feel it is very important to collect multi-component data and use the entire wavefield in the processing algorithm. In 2D, only the  $S_v$  mode is returned by the calculation of the curl operator in equation (6). In 3D, two horizontal component wavefields are also available. This leads to more possible cross-correlation images. The most obvious addition is combining two wavefields for an  $S_h$  wavefield. The total shear mode energy is captured by using the  $E_s$  in auto- or cross-correlations.

The methodology is sufficiently robust to tolerate irregular acquisition geometry and multiple sources in the wavefield. However, we have also shown that images are dependent on acquisition geometry, earth model and the source location, orientation and mechanism. The  $PP$ ,  $SS$  and  $PS$  imaging conditions we present will all respond differently to the convolution of these many parameters. Therefore, we advocate forward modelling a suite of source mechanisms with exact survey parameters to provide an interpretive dictionary with which to analyse the results from field data. The variation of focus characteristics in multiple images can provide the opportunity to interpret mechanism parameter information in addition to just source location. When recording only at the surface, the images from single forces versus double couple sources (Figs 9 and 10) will likely be difficult to distinguish in field data.

The imaging methodology, time-reverse imaging, we present is well suited to data with low signal content and complicated wave forms that may not be interpretable in the time data. As such, it is a powerful tool to locate and characterize sources or scatterers in the subsurface. The application of the method to subduction zone tremor (Shelly *et al.* 2007) is limited by the availability of accurate velocity models. Volcanic tremor data (Lokmer *et al.* 2009) may not suffer from

this problem. Continued development of this tool will help understand observations of tremor signals at the exploration scale (van Mastrigt and Al-Dulaijan 2008; Steiner *et al.* 2008; Saenger *et al.* 2009).

## ACKNOWLEDGEMENTS

Many thanks to Erik H. Saenger, Brian Steiner and Alex Goertz for fruitful discussions and helpful reviews and Spectraseis AG for permission to publish these tools. Patient reviewers helped scale back the heft and style of the paper to something approaching readable.

## REFERENCES

- Aki K. and Richards P.G. 2002. *Quantitative Seismology*, 2<sup>nd</sup> edn. University Science Books.
- Artman B. 2006. Imaging passive seismic data. *Geophysics* **71**, SI177–SI187.
- Artman B. and Podladtchikov I. 2009. Imaging conditions for time-reverse acoustics. EAGE Passive Seismic Workshop, 22–25 March, Limassol, Cyprus, Extended Abstracts, 168–174.
- Berkovitch A., Belfer I., Hassin Y. and Landa E. 2009. Diffraction imaging by multifocusing. *Geophysics* **74**, WCA75–WCA81. doi:10.1190/1.3198210
- Berryman J. 2002. Statistically stable ultrasonic imaging in random media. *Journal of Acoustical Society of America* **112**, 1509–1522.
- Borcea L., Papanicolaou G. and Tsogka C. 2003. Theory and applications of time reversal and interferometric imaging. *Inverse Problems* **19**, S134–S164.
- Borcea L., Papanicolaou G. and Tsogka C. 2006. Coherent interferometric imaging in clutter. *Geophysics* **71**, SI165–SI175. doi:10.1190/1.2209541
- Chambers K., Barkved O. and Kendall J.-M. 2009. Imaging induced seismicity with the lofs permanent sensor surface array. 79<sup>th</sup> SEG meeting, Houston, Texas, USA, Expanded Abstracts, 1612–1616.
- Chambers K., Brandsberg-Dahl S., Kendall J.-M. and Rueda J. 2008. Testing the the ability of surface arrays to locate microseismicity. 78<sup>th</sup> SEG meeting, Las Vegas, Nevada, USA, Expanded Abstracts, 1436–1440.
- Claerbout J. 1985. *Imaging The Earth's Interior*. Blackwell Scientific Publications.
- Claerbout J. 1992. *Earth Soundings Analysis*. Blackwell Scientific Publications.
- Claerbout J.F. 1971. Toward a unified theory of reflector mapping. *Geophysics* **36**, 467–481.
- Dellinger J.A., Nolte B. and Etgen J.T. 2001. Alford rotation, ray theory, and crossed-dipole geometry. *Geophysics* **66**, 637–647. doi:10.1190/1.1444954
- Dobrin M.B. 1952. *Introduction to Geophysical Prospecting*. McGraw-Hill.
- Dougherty M.E. and Stephen R.A. 1988. Seismic energy partitioning and scattering in laterally heterogeneous ocean crust. *Pure and Applied Geophysics* **128**, 195–229.
- Eshelby J.D. 1957. The determination of the elastic field of an ellipsoidal inclusion, and related problems. *Proceedings of the Royal Society of London. A. Mathematical and Physical Sciences* **241**, 376–396. doi:10.1098/rspa.1957.0133
- Feng X. and Sato M. 2004. Pre-stack migration applied to gpr for landmine detection. *Inverse Problems* **20**, S99–S115.
- Fink M. 1999. Time-reversed acoustics. *Scientific American* (November), 67–73.
- Fouque J.-P., Garnier J., Papanicolaou G. and Solna K. 2007. *Wave Propagation and Time Reversal in Randomly Layered Media*. Springer.
- Gajewski D. and Tessmer E. 2005. Reverse modelling for seismic event characterization. *Geophysical Journal International* **163**, 276–284.
- Gazdag J. and Sguazzero P. 1985. Migration of seismic data by phase shift plus interpolation. In: *Migration of Seismic Data*, pp. 3 23–330. SEG. (Reprinted from *Geophysics* **49**, 124–131).
- Grechka V., Mazumdar P. and Shapiro S.A. 2010. Predicting permeability and gas production of hydraulically fractured tight sands from microseismic data. *Geophysics* **75**, B1–B10. doi:10.1190/1.3278724
- Gutenberg B. and Richter C. 1954. *Seismicity of The Earth and Associated Phenomena*. Princeton University Press.
- Heaton T.H. and Heaton R.E. 1989. Static deformations from point forces and force couples located in welded elastic Poissonian half-spaces: Implications for seismic moment tensors. *Bulletin of the seismological society of America* **79**, 813–841.
- Huang J. and Milkereit B. 2007. Wave-equation-based separation of p- and s-wave modes. 77<sup>th</sup> SEG meeting, San Antonio, Texas, USA, Expanded Abstracts, 2135–2139.
- Jacobs B. 1982. *The prestack migration of profiles*. PhD thesis, Stanford University.
- Kawakatsu H. and Montagner J.-P. 2008. Time-reversal seismic-source imaging and moment-tensor inversion. *Geophysical Journal International* **175**, 686–688.
- Khaidukov V., Landa E. and Moser T.J. 2004. Diffraction imaging by focusing-defocusing: An outlook on seismic superresolution. *Geophysics* **69**, 1478–1490. doi:10.1190/1.1836821
- Lambert M.-A., Schmalholz S.M., Saenger E.H. and Steiner B. 2009. Reply to comment on 'low-frequency microtremor anomalies at an oil and gas field in Voitsdorf, Austria. *Geophysical Prospecting* **57**, 393–411.
- Levin S.A. 1984. Principle of reverse-time migration. *Geophysics* **49**, 581–583. doi:10.1190/1.1441693
- Lokmer I., O'Brien G.S., Stich D. and Bean C.J. 2009. Time reversal imaging of synthetic volcanic tremor sources. *Geophysical Research Letters* **36**, L12308.
- Maxwell S. and Urbancic T. 2001. The role of passive microseismic monitoring in the instrumented oil field. *The Leading Edge* **20**, 636–639.
- Maxwell S., White D. and Fabriol H. 2004. Passive seismic imaging of CO<sub>2</sub> sequestration at Weyburn. 74<sup>th</sup> SEG meeting, Denver, Colorado, Expanded Abstracts.

- Melton B.S. and Bailey L.F. 1957. Multiple signal correlators. *Geophysics* **22**, 565–588.
- Mefaxian J.P., Lesage P. and Dorel J. 1997. Permanent tremor of masaya volcano, nicaragua: Wave field analysis and source location. *Journal of Geophysical Research* **102**, 22529–22545.
- Morse P.M. and Feshbach H. 1953. *Methods of Theoretical Physics*. McGraw-Hill.
- Norton S.J. and Won I.J. 2000. Time exposure acoustics. *IEEE Transactions on Geoscience and Remote Sensing* **38**, 1337–1343. doi:10.1109/36.843027
- Riahi N., Kelly M., Ruiz M. and Yang W. 2009. Bayesian dhi using passive seismic low frequency data. 79<sup>th</sup> SEG meeting, Houston, Texas, USA, Expanded Abstracts, 1607–1611.
- Saenger E.H., Gold N. and Shapiro S.A. 2000. Modeling the propagation of elastic waves using a modified finite-difference grid. *Wave Motion* **31**, 77–92.
- Saenger E.H., Schmalholz S.M., Lambert M.-A., Nguyen T.T., Torres A., Metzger S., Habiger R.M., Müller T., Rentsch S. and Méndez-Hernández E. 2009. A passive seismic survey over a gas field: Analysis of low-frequency anomalies. *Geophysics* **74**, O29–O40. doi:10.1190/1.3078402
- Schubert F. and Schechinger B. 2002. Numerical modeling of acoustic emission sources and wave propagation in concrete. Available from: <http://www.ndt.net/article/v07n09/07/07.htm> (cited 26 Sept. 2009).
- Schuster G.T., Yu J., Sheng J. and Rickett J. 2004. Interferometric/daylight seismic imaging. *Geophysics Journal International* **157**, 838–852.
- Shelly D.R., Beroza G.C. and Ide S. 2007. Complex evolution of transient slip derived from precise tremor locations in western Shikoku, Japan. *Geochemistry Geophysics Geosystems* **8**, Q10014.
- Shragge J.C., Artman B. and Wilson C. 2006. Teleseismic shot-profile migration. *Geophysics* **71**, SI221–SI229.
- SMAART J.V. 2002. Joint Venture consisting of BHP Billiton, BP and ChevronTexaco. Available from: <http://www.delphi.tudelft.nl/SMAART> (cited 26 Sept. 2009).
- Steiner B. 2009. *Time reverse modeling of low-frequency tremor signals*. PhD thesis, Swiss Federal Institute of Technology Zurich.
- Steiner B., Saenger E.H. and Schmalholz S.M. 2008. Time reverse modeling of low-frequency microtremors: Application to hydrocarbon reservoir localization. *Geophysical Research Letters* **35**, L03307.
- van Mastrigt P. and Al-Dulaijan A. 2008. Seismic spectroscopy using amplified 3C geophones. 70<sup>th</sup> EAGE meeting, Rome, Italy, Extended Abstracts, B047.
- Vasconcelos I., Sava P. and Douma H. 2009. Wave-equation extended images via image-domain interferometry. 79<sup>th</sup> SEG meeting, Houston, Texas, USA, Expanded Abstracts, 2839–2843.
- Walters S.L., Miller R.D., Steeples D.W., Xia J. and Zeng C. 2009. Detecting tunnels and underground facilities using diffracted p-waves. *Symposium on the Application of Geophysics to Engineering and Environmental Problems* **22**, 937–942. doi:10.4133/1.3176787
- Wapenaar C.P.A., Kinneging N.A. and Berkhout A.J. 1987. Principle of prestack migration based on the full elastic two-way wave equation. *Geophysics* **52**, 151–173. doi:10.1190/1.1442291
- Yan J. and Sava P. 2008. Isotropic angle-domain elastic reverse-time migration. *Geophysics* **73**, S229–S239. doi:10.1190/1.2981241
- Yan J. and Sava P. 2009. Elastic wave-mode separation for VTI media. *Geophysics* **74**, WB19–WB32. doi:10.1190/1.3184014
- Yang T. and Sava P. 2009. Wave-equation migration velocity analysis using extended images. 79<sup>th</sup> SEG meeting, Houston, Texas, USA, Expanded Abstracts, 3715–3719.
- Zhe J. and Greenhalgh S.A. 1997. Prestack multicomponent migration. *Geophysics* **62**, 598–613. doi:10.1190/1.1444169
- Zhu X. and Wu R.-S. 2010. Imaging diffraction points using the local image matrices generated in prestack migration. *Geophysics* **75**, S1–S9. doi:10.1190/1.3277252